P-ISSN 2586-9000
E-ISSN 2586-9027
Homepage : *https://tci-thaijo.org/index.php/SciTechAsia*
Science & Technology Asia
Vol.27 No.1 January - March 2022
Page: [31-45]

Original research article

Modeling Investigations of Thermophoretic Magnetohydrodymics Flow in a Penetrable Wedge with Higher-Order Slip

M.M. Billah[1], Md. Khairul Alam[1], S. M. Chapal Hossain[2,*]

[1] *Department of Arts and Sciences, Ahsanullah University of Science and Technology, Dhaka 1208, Bangladesh*
[2] *Department of Applied Mathematics, University of Dhaka, Dhaka 1000, Bangladesh*

Received 16 April 2020; Received in revised form 6 March 2021
Accepted 22 March 2021; Available online 28 March 2022

ABSTRACT

Modeling studies were carried out to examine the thermophoretic magnetohydrodynamics flow phenomena in a penetrable wedge with the higher-order (second-order) slip interaction. The model problem including mass, momentum, and energy equations transforms into nonlinear ordinary differential equations by exploiting a new class of similarity approach. The modified model equations are solved using the Nachtsheim-Swigert shooting method with the sixth-order Runge-Kutta integration scheme. The numerical outputs generated for the stream function, velocity, and the local skin friction are equated with the past results presented in the literature and found to have excellent precision. The modeling results reveal that the velocity outlines drop gradually with the lessening of different model constraints comprising mass transfer coefficient, wedge angle, Prandtl number, Schmidt number, first-order slip parameters, and shrinkages with the intensification of second-order slip constraint. The outcomes also show that the temperature profiles rise with the upsurge of Biot number, and Schmidt number, whereas the reverse scenarios are observed for Hartmann number, and unsteadiness parameter. Numerical results for the effects of the distinct constraints named the local skin-friction coefficient, rate of heat and mass transfer, thermophoretic velocity, and thermophoretic deposition velocity are also exposed in tabular form and discussed in detail.

Keywords: Magnetohydrodynamics; Slip parameter; Shooting method; Thermophoresis

1. Introduction

When a tiny particle is suspended in a gas medium with a thermal gradient, it acquires a force that typically drives the particle from a high-temperature towards a cold one. Such a type of temperature variation is recognized as thermophoresis and has a vital role in several real-world applications, for example, air cleaning, heat exchanger, chemical vapor deposition, microelectronic

---

***Corresponding author:** chapal@du.ac.bd

manufacturing, nuclear reactor, catalysis-driven plasmonic nanomotor, soot particles removal from exhaust gas systems, microfluidic technologies (biochemical analyses, separation, and trapping), etc. [1-2]. Regardless of numerous uses, the fundamental mechanism of thermophoresis is still poorly understood, and it has been accepted as one of the unresolved difficulties in the arena of fluid mechanics [3].

Many factors are used to describe the thermophoresis phenomenon, such as the aerosol thermal conductivity, the gaseous heat capacity, the Knudsen number, and the thermophoretic coefficient. In these viewpoints, several studies focused on the characteristics of thermophoresis both numerically and experimentally. For instance, Chamkha and Issa [4] carried out a numerical experiment for investigating the influences of thermal creation or assimilation, as well as thermophoretic phenomena, over a smooth surface. Sohn et al. [5] reported on the radiating influence of thermophoretic gaseous particles. The steady laminar boundary layer flow phenomena in a flat plate with variable viscosity and Prandtl number was examined in the work of Pantokratoras [6]. He also focused on the convective boundary layer flow phenomena in a uniform plate case to explore the fluid viscosity deviation with heat. A numerical study investigated the speck deposition characteristics onto a frequently affecting curvy face in the work of Wang and Chen [7]. Their numerical outcomes revealed that the average deposition influence of the curvy face is larger than the smooth face. Postelnicu [8] clarified the thermophoretic speck deposition influence in a straight regular surface with porous media. Alam et al. [9] scrutinized the viscous dissipation and joule heating impacts on the hydromagnetic fluid flow in a slanted surface with the existence of thermophoresis. Rahman and Postelnicu [10] also explored the thermophoresis features of viscid fluid flow through a rotational object. Shehzad et al. [11] inspected the thermophoresis and heat emission approaches for Jeffry fluid flow case. All these studies concentrated on the thermophoretic features in distinct faces (e.g., slant face, straight face, smooth face, etc.), but none of them explore the magnetohydrodynamics flow features with thermophoretic interaction of different faces.

In addition, many investigators have paid much attention to the exploration of magnetohydrodynamics (MHD) fluid flow with different surfaces (e.g., wavy and flat faces) because of its significant uses in several scientific branches (e.g., physical science, medical science, and engineering) [12-13]. Soundalgekar and Murty [14] analyzed the MHD flow features. They solved the similarity equations and examined the different parameter impacts (suction/injection and pressure). Hossain and Ahmed [15] studied the combination of forced and natural convective boundary layer flow nearby the prime edge. Alam and Rahman [16] also examined the natural and forced convective characteristics flow in an upright penetrable plate and found that as the slip parameter increases, the slip velocity and the wall shear stress rise and drop, respectively. Sharma and Singh [17] reported on the variable suction and internal heat generation approaches for transient MHD flow and heat transfer with an upright porous face. Abel et al. [18] investigated the power-law fluid flow gesture in a perpendicular extending sheet with the existence of an irregular thermal source. Rahman et al. [19] introduce Buongiorno's numerical model and further scrutinized the nanofluid flow feature through a permeable lessening/elongating surface with higher-order slip constraint. On the other hand, Seddeek [20] investigated the radiative hydro-thermal characteristics in a constantly affecting porous frontier with different viscosity. Ali [21] evaluated the mixed convection thermal distributions in a perpendicular moving face variable with modified viscosity. Alam et al. [22] concentrated on the unsteady MHD natural convective fluid flow in a leaned absorbent plate with the manifestation of the unstable chemical reaction and temperature-dependent viscidness. Rahman et al. [23] studied the transient hydro-thermal flow occurrences in a wedge with different electric conductivity and thermophoresis. Gupta et al. [24] discussed the aspects of chemical reaction and radiation with the incompressible nanofluid flow and heat transfer over a leaned extending sheet. However, most of the explorations are focused on fluid flow through different surfaces include wavy and flat surfaces but few works seem to be done to investigate thermophoretic magnetohydrodynamics flow through a wedge surface.

The goal of the modeling study is to numerically examine the thermophoretic magnetohydrodynamics flow occurrences in a penetrable wedge with the higher-order (second-order) slip interaction. The mathematical model equations involving mass, momentum, and energy equations transform into nonlinear ordinary differential equations by exploiting a new class of similarity variables as proposed by Sattar [25]. The modified model equations are then solved using the Nachtsheim-Swigert shooting method with the sixth-order Runge-Kutta integration scheme. The numerical outputs are exposed through graphs and tables with different parameter effects and further discussed in detail.

2. Computational Methodology

2.1 Mathematical model

The hydrothermal flow events are pondered in a penetrable wedge with the higher-order (second-order) slip interaction. The flow is anticipated to be transient, laminar, viscous, incompressible, and two-dimensional (2D) when the wedge angle is chosen as $\Omega = \beta\pi$ along the x-axis and the y-axis normal to it. The wedge face is kept at the uniform constant temperature (T_f), and concentration (C_w), respectively, that are larger than the ambient temperature (T_∞), and concentration (C_∞), respectively. Also, the magnetic field strength (B_0) is settled parallel to the y-axis and the fluid suction/injection approach is employed on the wedge face as depicted in Fig. 1. Thus, the major model equations are as follows [15-16, 22-23].

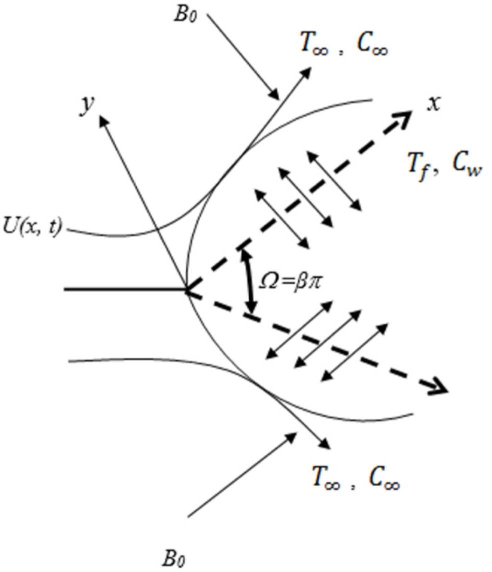

Fig. 1. Physical illustrations of the problem.

$$\frac{\partial u}{\partial x} + \frac{\partial v}{\partial y} = 0, \tag{2.1}$$

$$\frac{\partial u}{\partial t} + u\frac{\partial u}{\partial x} + v\frac{\partial u}{\partial y} = \frac{\partial U}{\partial t} + U\frac{\partial U}{\partial x} \tag{2.2}$$

$$+\upsilon\frac{\partial^2 u}{\partial y^2} - \frac{\sigma {B_0}^2}{\rho}(u-U),$$

$$\frac{\partial T}{\partial t} + u\frac{\partial T}{\partial x} + v\frac{\partial T}{\partial y} = \frac{k_g}{\rho c_p}\frac{\partial^2 T}{\partial y^2} \tag{2.3}$$

$$+\frac{\mu}{\rho c_p}\left(\frac{\partial u}{\partial y}\right)^2 + \frac{\sigma {B_0}^2}{\rho c_p}(u-U)^2,$$

$$\frac{\partial C}{\partial t} + u\frac{\partial C}{\partial x} + v\frac{\partial C}{\partial y} = D\frac{\partial^2 C}{\partial y^2} - \frac{\partial}{\partial y}(V_T C), \tag{2.4}$$

where u and v, the velocity components in the x-, and y-directions respectively; t, the time; $\upsilon(=\frac{\mu}{\rho})$, the kinematic viscosity altered from 1.516×10^{-5} m^2 s^{-1} to 1.004×10^{-6} m^2 s^{-1} [25-26]; ρ, the fluid density; μ, the dynamic viscosity of the fluid; T, the temperature; C, the concentrations; $k_g\,(=3.75\mu R)$, the thermal conductivity of the fluid [26]; R, specific gas constant of fluid; D, the diffusivity of the species concentration; and $\kappa\upsilon$, the thermophoretic diffusivity. The thermophoretic velocity [26] is defined as:

$$V_T=\frac{\kappa\upsilon}{T}\frac{\partial T}{\partial y}. \tag{2.5}$$

The thermophoretic coefficient ranging from 0.2 to 1.2 [27] is expressed as:

$$\kappa=\frac{2C_s(k_g/\lambda_p+C_tKn)C_c}{(1+3C_mKn)(1+2k_g/\lambda_p+2C_tKn)}, \tag{2.6}$$

where k_g, and λ_p are the thermal conductivities of the fluid and diffused particles, respectively; $C_m=1.146, C_s=1.147$, $C_t=2.2$ are the fixed parameters acquired from the experimental data.

The Stokes-Cunningham correction factor is

$$C_c=[1+Kn(C_1+C_2e^{-C_3/Kn})], \tag{2.7}$$

where $C_1=1.2, C_2=0.41, C_3=0.88$, the Knudsen number $Kn\,(=\xi/r)$ is varied from 0.07 to 0.15 [26]; the mean free path is ξ and the particle radius is $r\,(=1\mu m)$.

The model boundary conditions are given below:

(i) At the wedge face $(y=0)$

$$u=\lambda_1U+A\frac{\partial u}{\partial y}+B\frac{\partial^2u}{\partial y^2},\ v=\pm v_w(x,t), \tag{2.8}$$
$$-k_g\frac{\partial T}{\partial y}=h_f(T_f-T);\ C=C_w;$$

(ii) At free stream case $(y\to\infty)$

$$u=U(x,t), T=T_\infty, C=C_\infty \tag{2.9}$$

where $U(x,t)=\upsilon x^m/\delta^{m+1}$, the wedge flow velocity [28]; m, the arbitrary constant, and $\delta=\delta\,(t)$, the length scale [28-30].

2.2 Similarity approach

The following non-dimensional variables are preferred to modify the key model Eqs. (2.1-2.4) with the boundary conditions as presented in Eqs. (2.8-2.9) [29]:

$$\eta=y\sqrt{\frac{m+1}{2}}\sqrt{\frac{x^{m-1}}{\delta^{m+1}}},$$
$$\psi=\sqrt{\frac{2}{m+1}}\frac{\upsilon x^{\frac{m+1}{2}}}{\delta^{\frac{m+1}{2}}}f(\eta), \tag{2.10}$$
$$\theta(\eta)=\frac{T-T_\infty}{T_f-T_\infty};\varphi(\eta)=\frac{C-C_\infty}{C_w-C_\infty}.$$

The following correlations are gotten using $u=\partial\psi/\partial y$, and $v=-\partial\psi/\partial x$, where ψ is the stream function:

$$u=U(x,t)f'$$
$$v=-\sqrt{\frac{2}{m+1}}\left(\frac{m+1}{2}\right)\upsilon\sqrt{\frac{x^{m-1}}{\delta^{m+1}}}\left[f+\frac{m-1}{m+1}\eta f'\right]. \tag{2.11}$$

Finally, the resulting model equations are obtained with the help of Eqs. (2.10-2.11) as follows:

$$f'''+ff''+\beta(1-f'^2)-2\lambda(1-f')$$
$$+\lambda\eta f''-\frac{2}{m+1}Ha^2(f'-1)=0, \tag{2.12}$$

$$\theta''+\Pr\lambda\eta\theta'+\Pr f\theta'+\Pr Ec(f'')^2$$
$$+Ha^2\Pr Ec(f'-1)^2=0, \tag{2.13}$$

$$\varphi''+Sc\lambda\eta\varphi'+Scf\varphi'$$
$$+\frac{\kappa Sc}{Nt+\theta}\{(Nc+\varphi)\theta''+\theta'\varphi'\} \tag{2.14}$$
$$-\frac{\kappa Sc}{Nt+\theta}\frac{Nc+\varphi}{Nt+\theta}(\theta')^2=0$$

with

$$f = f_w,\ f' = \lambda_1 + af'' + bf''',$$
$$\theta' = Bi(\theta - 1), \varphi = 1 \ \text{ at } \eta = 0, \qquad (2.15)$$
$$f' = 1,\quad \theta = 0,\quad \varphi = 0 \quad as\ \eta \to \infty, \qquad (2.16)$$

where f, the dimensionless stream function; $\beta = \frac{2m}{m+1}$, the wedge angle; $\Pr = \frac{\mu c_p}{\kappa}$, the Prandtl number; $Ha = B_0\sqrt{\frac{\sigma x}{\rho U}}$, the Hartmann number; $Ec = \frac{U}{c_p(\mathrm{T_w} - \mathrm{T_\infty})}$, the Eckert number; $Sc = \frac{\nu}{D}$, the Schmidt number; $Nt = \frac{T_\infty}{\mathrm{T_w} - \mathrm{T_\infty}}$, the thermophoresis parameter; $Nc = \frac{C_\infty}{C_w - C_\infty}$, the concentration ratio; $f_w = -\frac{v_w(x,t)}{\sqrt{\frac{m+1}{2}\upsilon}\sqrt{\frac{x^{m-1}}{\delta^{m+1}}}}$, the wall mass transfer coefficient; the Prime specifies differentiation with respect to η.

2.3 Data analysis

To analyze the numerical data, it is crucial to find out several physical parameters that are specified by the following relationships:

$$C_{fx} = \frac{\tau_w}{\frac{1}{2}\rho U^2},\ Nu_x = \frac{q_w x}{k_g(T_f - T_\infty)},$$
$$Sh_x = \frac{M_w x}{D(C_w - C_\infty)},\ V_d = \left[\frac{M_w}{(C_w - C_\infty)}\right]_{y=0}, \qquad (2.17)$$

where τ_w is the wall shear stress on the surface; q_w the heat transfer rate; and M_w the mass transfer rate, which are determined as follows:

$$\tau_w = \mu\left(\frac{\partial u}{\partial y}\right)_{y=0},\ q_w = -k_g\left(\frac{\partial T}{\partial y}\right)_{y=0},$$
$$M_w = -D\left(\frac{\partial C}{\partial y}\right)_{y=0}. \qquad (2.18)$$

Table 1. Physical factors used in numerical results analysis [15-16, 22-23, 25].

Items	Correlations
Skin-friction	$\frac{1}{2}C_{fx}\sqrt{2-\beta} = \mathrm{Re}^{-\frac{1}{2}} f''(0)$
Nusselt number	$Nu_x\sqrt{2-\beta} = -\mathrm{Re}^{\frac{1}{2}}\theta'(0)$
Sherwood number	$Sh_x\sqrt{2-\beta} = -\mathrm{Re}^{\frac{1}{2}}\varphi'(0)$
Thermophoretic velocity	$V_{Tw} = -\sqrt{\frac{1}{2-\beta}}\frac{1}{Sc}\mathrm{Re}^{\frac{1}{2}}\frac{\kappa}{1+Nt}\theta'(0)$
Thermophoretic particle deposition velocity	$V_d{}^* = -\sqrt{\frac{1}{2-\beta}}\frac{1}{Sc}\mathrm{Re}^{\frac{1}{2}}\varphi'(0)$

Now putting Eqs. (2.11) and (2.18) into Eq. (2.17), the resulting physical parameters are obtained to examine the numerical outcomes as shown in Table 1.

3. Numerical Scheme and Validation

The modified model Eqs. (2.12)-(2.14) with (2.15)-(2.16) have been solved numerically with the aid of the Nachtsheim-Swigert shooting iteration procedure with the sixth-order Runge-Kutta integration outline [31]. During the numerical study, the step size, $\Delta\eta = 0.1$, was adopted to be agreeable for convergence criteria less than 10^{-6} in all cases and obtained the value of η_∞ in each iteration by $\eta_\infty = \eta_\infty + \Delta\eta$ [26, 31]. The highest values, η_∞, are gotten for each set of factors $\beta, \lambda, \kappa, \Pr, Ec, Sc, Ha, Nc,$ and Nt when the values of η are assumed to be zero [22-23, 26, 31].

The numerical values of $f(\eta)$, $f'(\eta)$, and $f''(\eta)$ are acquired in the present work with $\beta = 0$, and $\lambda = 0$, which are compared with the results of White [32] as tabulated in Table 2. It is clearly observed from Table 2 that the outputs made by the current study and the work of White [32] are found to be in excellent agreement.

Table 2. Comparison results of the present numerical study and the former study of White [32].

η	$f(\eta)$		$f'(\eta)$		$f''(\eta)$	
	Present results	White [32]	Present results	White [32]	Present results	White [32]
0.0	0.0000	0.0000	0.0000	0.0000	0.4690	0.4696
0.5	0.0593	0.0586	0.2354	0.2342	0.4565	0.4650
1.0	0.2422	0.2329	0.4563	0.4606	0.4376	0.4343
1.5	0.5157	0.5150	0.6623	0.6614	0.3621	0.3618
2.0	0.9011	0.8868	0.8255	0.8166	0.2643	0.2556
3.0	1.8098	1.7955	0.9860	0.9690	0.0783	0.0677
4.0	2.7953	2.7838	0.9998	0.9977	0.0069	0.0068
5.0	3.8005	3.7832	1.0009	0.9999	0.0002	0.0002

4. Results and Discussion

The aim of this study is to numerically scrutinize the thermophoretic MHD flow incidents in a penetrable wedge face with the second-order slip interaction. The transformed model equations with the altered boundary conditions have been solved numerically using the shooting method [31]. The results of velocity, temperature, and concentration are revealed in the graphic outlook and discussed elaborately under the impacts on distinct factors. The numerical results of the skin-friction coefficient, rate of heat and mass transfer, thermophoretic velocity, and thermophoretic particle deposition velocity are shown in table format for various values of model constraints as well. More specifically, the different values of Prandtl number, Pr = 0.71, 1, 2.97, 4.24, and 7.02, are chosen at the time of the numerical modeling study, that correspond to air, electrolyte solution such as saltwater, methyl chloride, sulfur dioxide and water at $20^0 C$. The other parameter values have been taken as the mass transfer coefficient, $f_w = 0.5$; Hartmann number, $Ha = 2$; unsteadiness parameter, $\lambda = 1.5$; concentration ratio , $Nc = 2$; thermophoresis parameter, $Nt = 2$; wedge angle parameter, $\beta = 0.2$; thermophoretic coefficient, $\kappa = 0.2$; Biot number, $Bi = 5$; the first order slip parameter, $a = 2$; the second order slip parameter, $b = -0.2$ unless otherwise specified.

The modeling results are shown in Fig. 2 for several values of the mass transfer coefficient (f_w), that illustrate the typical profiles of velocity ($f'(\eta)$), temperature ($\theta(\eta)$), and concentration ($\varphi(\eta)$).

In Fig. 2 (a), it is revealed that the velocity outlines, $f'(\eta)$ fall gradually with the drop of mass transfer co-efficient f_w.

Fig. 2(b) exposed that the thermal profiles, $\theta(\eta)$, rise progressively with the decline of mass transfer co-efficient f_w .

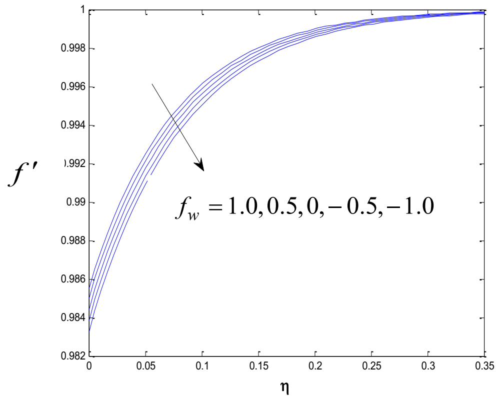

(a)

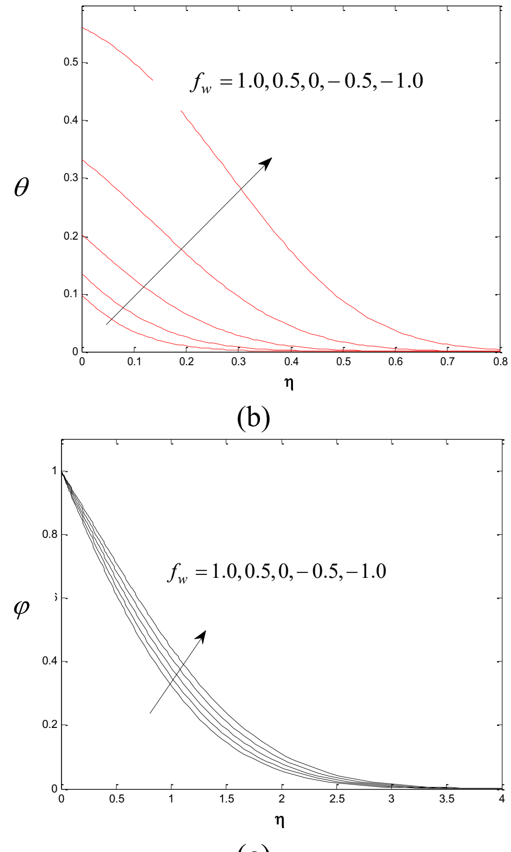

(b)

(c)

Fig. 2. Modeling results for several values of the mass transfer coefficient (f_w). (a) Velocity profiles, (b) Temperature profiles, and (c) Concentration profiles.

From Fig. 2(c), it is seen that the concentration profiles, $\varphi(\eta)$, increase moderately with decreasing values of mass transfer coefficient f_w.

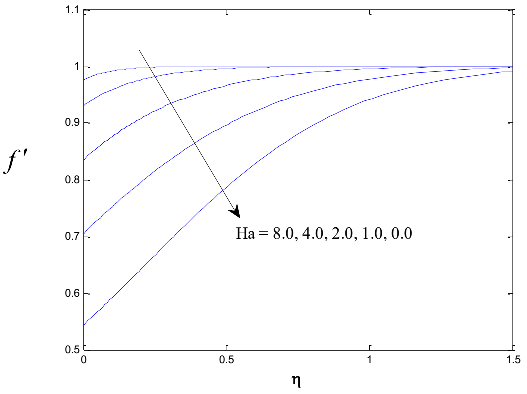

(a)

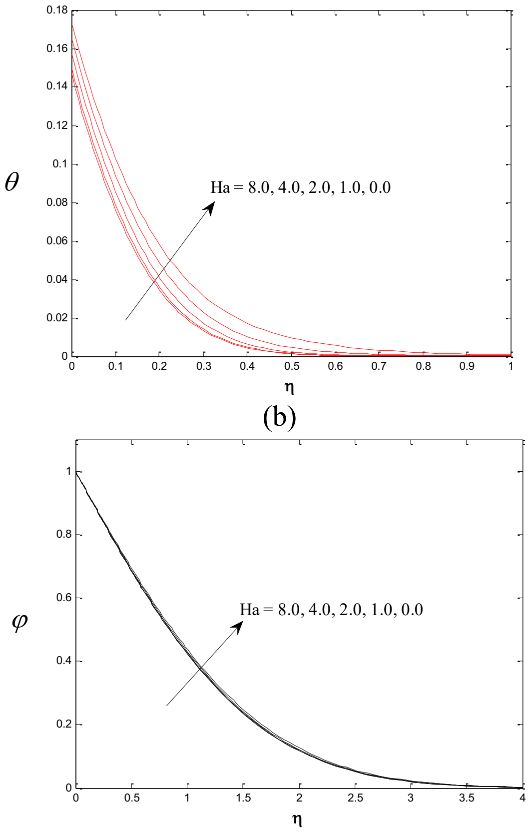

(b)

(c)

Fig. 3. Modeling results for different values of Hartmann number (*Ha*). (a) Velocity profiles, (b) Temperature profiles, and (c) Concentration profiles.

It can further be noted that the effect of the velocity and the temperature as well as the concentration of the fluid are consistent with the work of Rahman et al. [29].

Figs. 3(a)-(c) depicts the modeling results of velocity, temperature, and concentration outlines, respectively, with different values of Hartmann number (*Ha*). It is observed from Fig. 3(a) that the outlines of velocity increase with the improvement of magnetic field *Ha*. The reason is that the application of a magnetic field moving with the free stream tends to accelerate the electromotive force, which further intensifies the fluid motion.

From Fig. 3(b), it is noticed that temperature profiles decline moderately with the falling of *Ha*.

In addition, the results depicted in Fig. 3(c) exhibit that the concentration profiles, $\varphi(\eta)$ shrink slightly with the decreasing values of Ha.

It can further be noted that the thicknesses of the thermal and concentration boundary layers decrease with the increase of the strength of the applied magnetic field that is consistent with the work of Rahman et al. [29]

Numerical results for various values of Prandtl number (Pr) are presented in Figs. 4(a)-(c). From Fig. 4(a), it is observed that the typical velocity drops very slowly by lessening the values of Pr.

It is found from Fig. 4(b) that the profiles of temperature decline moderately with the decreasing values of Pr ranging from 7.02 to 0.71.

Also, the concentration profile of the fluid depicted in Fig. 4(c) within the boundary layer increases very slightly with the sinking of the Prandtl number.

Figs. 5(a)-(c) demonstrated the typical profiles of $f'(\eta)$, $\theta(\eta)$, and $\varphi(\eta)$ for different values of the unsteadiness parameter (λ). It is observed from Fig. 5 (a) that the velocity profiles $f'(\eta)$ decrease gradually with the decreasing values of the unsteadiness parameter λ ranging from 2.5 to 0.5.

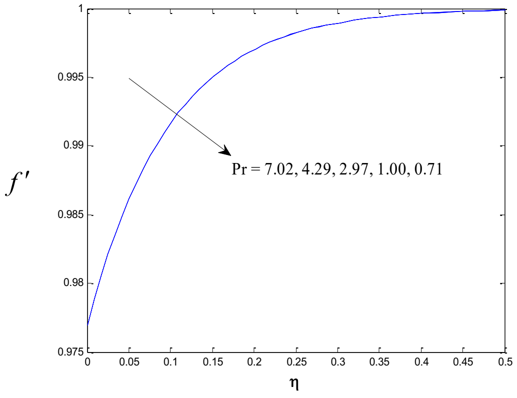

(a)

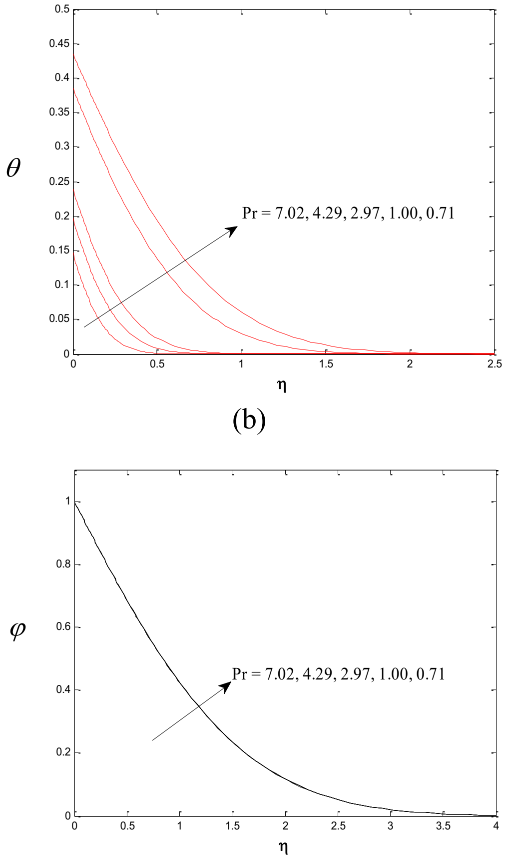

(b)

(c)

Fig. 4. Numerical results for various values of Prandtl number (Pr). (a) Velocity profiles, (b) Temperature profiles, and (c) Concentration profiles.

The numerical results displayed in Fig. 5(b) show that the profiles of temperature diminish moderately with the decreasing values of λ ranging from 2.5 to 0.5.

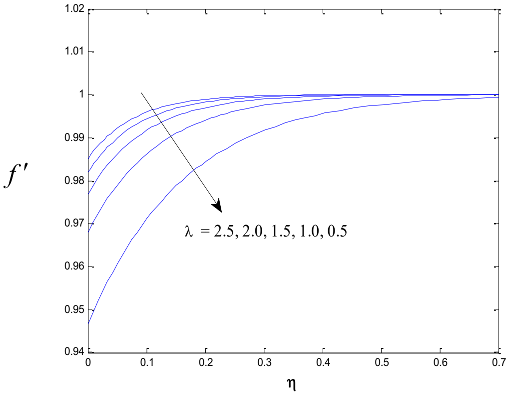

(a)

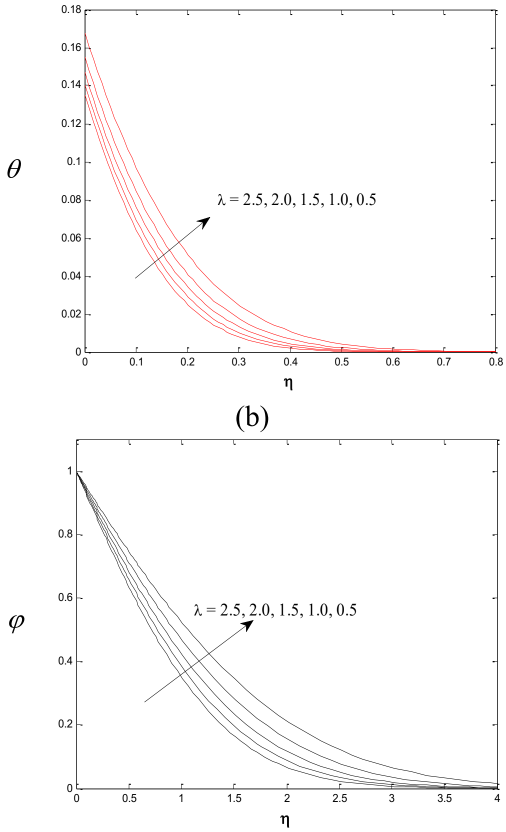

(b)

(c)

Fig. 5. Typical profiles of (a) Velocity, (b) Temperature, and (c) Concentration for different values of the unsteadiness parameter (λ).

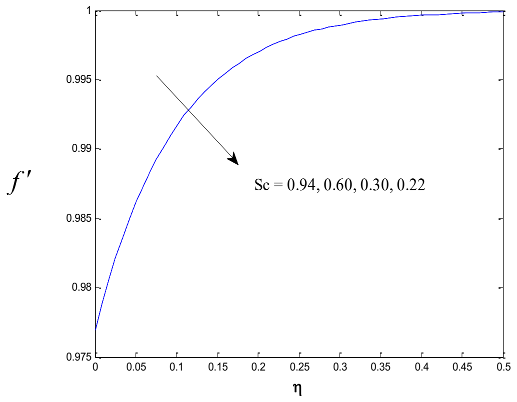

(a)

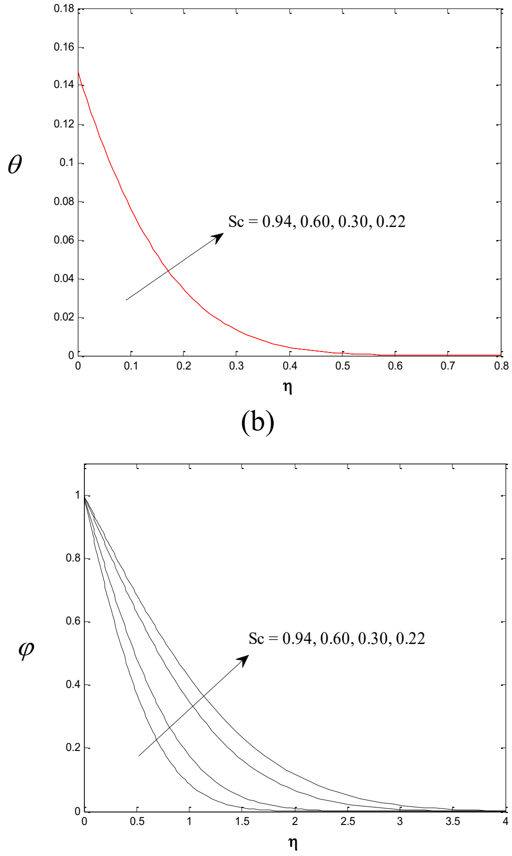

(b)

(c)

Fig. 6. Typical profiles of (a) Velocity, (b) Temperature, and (c) Concentration for distinct values of the Schmidt number (*Sc*).

Besides, it is observed that the computational results of the non-dimensional concentration sketches decrease steadily while reducing the values of the unsteadiness parameter λ from 2.5 to 0.5 in Fig. 5(c).

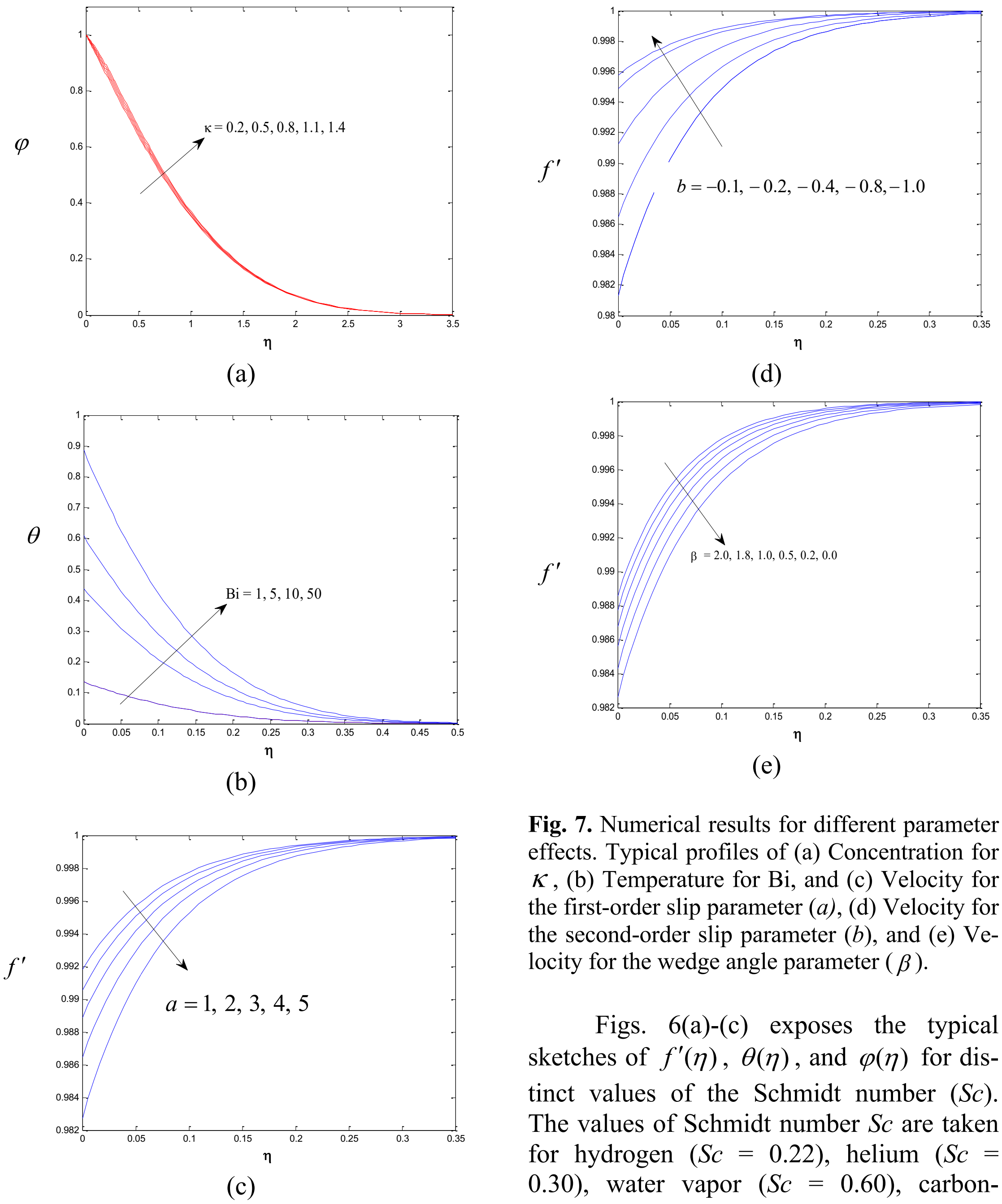

(a)

(b)

(c)

(d)

(e)

Fig. 7. Numerical results for different parameter effects. Typical profiles of (a) Concentration for κ, (b) Temperature for Bi, and (c) Velocity for the first-order slip parameter (*a*), (d) Velocity for the second-order slip parameter (*b*), and (e) Velocity for the wedge angle parameter (β).

Figs. 6(a)-(c) exposes the typical sketches of $f'(\eta)$, $\theta(\eta)$, and $\varphi(\eta)$ for distinct values of the Schmidt number (*Sc*). The values of Schmidt number *Sc* are taken for hydrogen (*Sc* = 0.22), helium (*Sc* = 0.30), water vapor (*Sc* = 0.60), carbondioxide (*Sc* = 0.94) during numerical investigations as well. It is revealed from Fig. 6(a) that the velocity outlines named $f'(\eta)$ reduce very slightly by the shrinkage of *Sc*.

In Fig. 6(b), it is noticed that when the numerical values of *Sc* diminished from 0.94 to 0.22, then the non-dimensional temperature outlines named $\theta(\eta)$ upturn very slightly.

The influence of Schmidt number *Sc* on the concentration profiles named $\varphi(\eta)$ escalate moderately with the decrease of *Sc* as viewed in Fig. 6 (c). It is noticed that the high concentration is found for hydrogen.

Numerical results for different parameter effects are illustrated in Figure 7. Fig. 7(a) depicted the effects of the thermophoretic co-efficient (κ) on the outlines of $\varphi(\eta)$. It is observed that the outlines of $\varphi(\eta)$ increase slightly with the increasing values of κ ranging from 0.2 to 1.4.

Fig. 7(b) demonstrates the influence of the Biot number (*Bi*) on the profiles of $\theta(\eta)$ and found that the outlines rise moderately with the upturn of *Bi* which is consistent with the work of Alam et al. [9]. The surface convection parameter or Biot number is a ratio of the hot fluid side convection resistance to the cold fluid side convection resistance on a surface. For fixed cold fluid properties and fixed free stream velocity, the surface convection parameter (Bi) at any station is directly proportional to the heat transfer coefficient h_f associated with the cold fluid. The thermal resistance on the hot fluid side is inversely proportional to h_f. As (Bi) increases, the hot fluid side convection resistance decreases and consequently, the surface temperature increases. From this figure it also confirmed that for large values of (Bi) i.e $(Bi \to \infty)$, the temperature profile attains its maximum value 1. From the convection boundary condition become the prescribed surface temperature case. It also is revealed from this graph that there is a peak value of $\theta(\eta)$ for large numerical values of *Bi*.

Fig. 7(c) exhibited the first-order slip constraint (*a*) impacts on the profiles of $f'(\eta)$ and found that the graphic trends of $f'(\eta)$ decreased reasonably with the rising values of *a* ranging from 1 to 5. This behavior is consistent with the works of Alam et al [9]

Fig. 7(d) illustrates the higher-order (second-order) slip factor (*b*) influence on the sketches of $f'(\eta)$ and shows that the outlines of $f'(\eta)$ increase with the declining numerical values of *b*. It is also noticed that this performance is in agreement with Alam et al [9]. The trend of this figure is just the reverse of Fig. 7 (c) and hence, the different slip constraints (i.e., *a*, and *b*) specify a vital role in demonstrating the flow incidents in a stretching/shrinking surface.

Fig. 7(e) plots the profiles of $f'(\eta)$ for the different wedge angle constraints (β) and found that the outlines of $f'(\eta)$ decreased rationally while reducing the numerical values of β. The outcomes also revealed that the profiles of $f'(\eta)$ became steeper for the bigger values of β. The constraint named β also correlated with the characteristics of the pressure gradient, and so the non-negative values of β identify non-positive pressure gradient occurrences, and consequently the outlines of $f'(\eta)$ squeeze nearby the wedge surface and the features of backflow do not occur.

Table 3. Numerical results for $f''(0)$, $-\theta'(0)$, $-\phi'(0)$, $V_{TW}\,\mathrm{Re}^{-\frac{1}{2}}$, $V_d^*\,\mathrm{Re}^{-\frac{1}{2}}$ with different Hartmann numbers.

f_w	Ha	$f''(0)$	$-\theta'(0)$	$-\varphi'(0)$	$V_{TW}\,\mathrm{Re}^{-\frac{1}{2}}$	$V_d^*\,\mathrm{Re}^{-\frac{1}{2}}$
0.5	0.0	0.244407071328291	2.81325518769666	0.623349432380901	0.153134216135434	2.31346672846475
0.5	1.0	0.228880714585091	2.78209045418041	0.634028595416207	0.151437822911331	2.35310081985337
0.5	2.0	0.213607316620888	2.80188076887845	0.638322797630021	0.152515071197093	2.36903809905969
0.5	4.0	0.177542015899373	2.80873462440110	0.639449272941815	0.152888147837121	2.37321884106233
0.5	8.0	0.130072058579863	2.81130182570187	0.639675641220085	0.153027888576097	2.37405897254068
-0.5	0.0	0.377248341008000	1.57366050961726	0.622590790595059	0.085659228376231	2.31065114471798
-0.5	1.0	0.221299820903953	1.39749312638118	0.587263071044951	0.076069890637348	2.17953768006054
-0.5	2.0	0.217179219573717	1.41551950354189	0.589035614690477	0.077051122325231	2.18611620654289
-0.5	4.0	0.182343987656103	1.43316181840912	0.590284241599750	0.078011448309813	2.19075029564414
-0.5	8.0	0.132877207694092	1.43865135390685	0.590437032773123	0.078310260774132	2.19131735687439

Table 4. Numerical results for $f''(0)$, $-\theta'(0)$, $-\phi'(0)$, $V_{TW}\,\mathrm{Re}^{-\frac{1}{2}}$, $V_d^*\,\mathrm{Re}^{-\frac{1}{2}}$ with different Biot numbers.

f_w	Bi	$f''(0)$	$-\theta'(0)$	$-\varphi'(0)$	$V_{TW}\,\mathrm{Re}^{-\frac{1}{2}}$	$V_d^*\,\mathrm{Re}^{-\frac{1}{2}}$
0.5	1.0	0.179349166539681	0.865003671554806	0.724886925610661	0.0470848360209619	2.69030771054689
0.5	5.0	0.179349166593493	2.810662564224789	0.639683053313139	0.1529930915887391	2.37408648139309
0.5	10	0.179349166593494	3.910015863492471	0.600727830727647	0.2128343055943182	2.22951009026294
0.5	50	0.179349166594572	5.690684273346049	0.547978436504961	0.3097616168217489	2.03373872649282
-0.5	1.0	0.181910083073491	0.668219236280734	0.608466610452431	0.0363732481155571	2.25823139565742
-0.5	5.0	0.181910083188658	1.437542055997691	0.590463094381846	0.0782498782441285	2.19141408057628
-0.5	10	0.181910083189682	1.679200652257629	0.586104464243119	0.0914041060839958	2.17523768691353
-0.5	50	0.181910083189708	1.940115825481765	0.586104464243112	0.1056065292073082	2.15975627704247

Table 3 shows the numerical results for $f''(0)$, $-\theta'(0)$, $-\phi'(0)$, $V_{TW}\,\mathrm{Re}^{-\frac{1}{2}}$, $V_d^*\,\mathrm{Re}^{-\frac{1}{2}}$ with different Hartmann numbers (*Ha*) for both suction $(f_w > 0)$ and injection $(f_w < 0)$ cases. It is seen that the numerical results of $f''(0)$ decreased slightly, to 46.78% and 64.78% in the case of suction and injection, respectively, while changing the numerical values of Ha from 0.0 to 8.0 for $f_w > 0$, and $f_w < 0$. The outcomes of $-\varphi'(0)$ augmented slightly with the increase of *Ha* for $f_w > 0$, and $f_w > 0$, respectively. The outputs also reveal that the thermophoretic particle deposition velocity rises and declines by 2.62% and 5.16%, respectively, with the upturn of *Ha* for $f_w > 0$, and $f_w > 0$. The non-dimensional thermophoretic velocity also declines with the upsurge of *Ha* for both cases.

Table 4 clarifies the numerical results of $f''(0)$, $-\theta'(0)$, $-\phi'(0)$, $V_{TW}\,\mathrm{Re}^{-\frac{1}{2}}$, $V_d^*\,\mathrm{Re}^{-\frac{1}{2}}$ with different Biot numbers (*Bi*) for both suction $(f_w > 0)$ and injection $(f_w < 0)$ circumstances. It can be seen that the results of $f''(0)$ and $-\theta'(0)$ are highly increased while increasing the values of *Bi* for both $f_w > 0$, and $f_w > 0$. Also, the computed values of $-\varphi'(0)$ decrease with the rising values of the constraint named *Bi* for $f_w > 0$, and $f_w > 0$ scenerios. The non-dimensional thermophoretic velocity rises significantly with the augmenting values of *Bi* for both incidents. The computed outputs also disclose that the thermophoretic particle deposition velocity shrinks steadily, which was 24.40% and 4.36% while amplifying the numerical values of *Bi* for both $f_w > 0$ and $f_w > 0$.

5. Conclusions

In this study, the influence of thermophoretic particle deposition on unsteady forced convective heat and mass transfer flow along a permeable wedge has been analyzed numerically. During the investigations, the major findings are as follows:

(i) The velocity outlines shrinkage reasonably with the decline of all parameters except higher-order slip constraint effects.

(ii) The temperature outlines improve reasonably with the improvement of the Schmidt number and Biot number, whereas the reverse scenarios are observed for the Hartmann number, mass transfer coefficient, and Prandtl number.

(iii) The concentration profiles increase steadily while declining the numerical values of the mass transfer coefficient, the Prandtl number, and the Schmidt number, and also reduce moderately with the reduction of the Hartmann number and the unsteadiness constraint.

(iv) The heat transfer rate increases with the increase of Schmidt number and unsteadiness parameter.

(v) The mass transfer rate significantly increases with the increase of the Schmidt number.

(vi) The thermophoretic particle deposition velocity decreases with the increase of Schmidt number, Hartmann number, and Biot number but decreases of mass transfer coefficients.

Finally, it is predicted that the presented numerical works could be used as a vehicle for understanding the thermophoresis particle deposition on MHD heat and mass transfer approach as revealed by unsteady laminar convective boundary layer flows along with a permeable wedge in the presence of a magnetic field.

Nomenclature

a	First order slip parameter,
b	Second order slip parameter,
Bi	Biot number,
Ec	Eckert number,
Ha	Hartmann number,
k_g	Thermal conductivity (W m^{-1} K^{-1}),
R	Specific gas constant (J mol^{-1} K^{-1}),
Nc	concentration ratio,
Nt	thermophoresis parameter,
Pr	Prandtl number,
Re	Reynolds number,
Sc	Schmidt number,
U	free steam velocity (m s^{-1}).

Greek symbols

α	Thermal diffusivity (m^2 s^{-1}),
β	Wedge angle parameter,
δ	Time dependent length scale,
μ	Dynamic viscosity (kg m^{-1} s^{-1}),
λ	Unsteadiness parameter,
θ	Non-dimensional fluid temperature,
υ	Kinematic viscosity (m^2 s^{-1}),
ρ	Gensity of the fluid (kg m^{-3}),
κ	Thermophoretic coefficient,
ϕ	Dimensionless concentration.

References

[1] Sasse AGBM, Nazaroff WW, Gadgil AJ. Particle Filter Based on Thermophoretic Deposition from Natural Convection Flow. Aerosol Science and Technology. 1994;20:227-38.

[2] Montassier N, Boulaud D, Renoux A. Experimental study of thermophoretic particle deposition in laminar tube flow. Journal of Aerosol Science. 1991;22:677-87.

[3] Brenner H, Bielenberg JR. A continuum approach to phoretic motions: Thermophoresis. Physica A: Statistical Mechanics and its Applications. 2005;355:251-73.

[4] Chamkha A, Issa C. Effects of heat generation/absorption and thermophoresis on hydromagnetic flow with heat and mass transfer over a flat surface. International Journal of Numerical Methods for Heat and Fluid Flow. 2000;10:432-49.

[5] Sohn Y, Baek S, Kim D. Thermophoresis of Particles in Gas-Particle Two-Phase Flow with Radiation Effect. Numerical Heat Transfer Part A-applications. 2002;41:165-81.

[6] Pantokratoras A. Forced and mixed convection boundary layer flow along a

flat plate with variable viscosity and variable Prandtl number: new results. Heat and Mass Transfer. 2005;41:1085-94.

[7] Wang CC, Chen CK. Thermophoretic deposition of particles from a boundary layer flow onto a continuously moving wavy surface. Acta Mechanica. 2006;181:139-51.

[8] Postelnicu A. Effects of thermophoresis particle deposition in free convection boundary layer from a horizontal flat plate embedded in a porous medium. International Journal of Heat and Mass Transfer. 2007;50:2981-5.

[9] Alam MS, Haque M, Uddin M. Convective flow of nanofluid along a permeable stretching/shrinking wedge with second order slip using Buongiorno's mathematical model. Int. J. Adv. Appl. Math. and Mech. 2016;3(3):79-91.

[10] Rahman MM, Postelnicu A. Effects of thermophoresis on the forced convective laminar flow of a viscous incompressible fluid over a rotating disk. Mechanics Research Communications. 2010;37:598-603.

[11] Shehzad S, Hayat T, Alsaedi A, Ahmad B. Effects of thermophoresis and thermal radiation in mixed convection three-dimensional flow of Jeffrey fluid. Applied Mathematics and Mechanics. 2015;36:655-68.

[12] Bhaskar K, Sharma K, Gupta S, Mehta R. MHD Fluid Flow with Cross-Diffusion Effects through Channel Using Optimal Homotopy Analysis Method. Science & Technology Asia. 2020;25:19-30.

[13] Mehta T, Mehta R, Kumar D. Unsteady Magnetohydrodynamic Flow in the Presence of Permeable Medium through an Upstanding Channel with Persistent Suction and Heat Source. Science & Technology Asia. 2020;25:106-22.

[14] Soundalgekar VM, Murty TVR. Heat transfer in MHD flow with pressure gradient, suction and injection. Journal of Engineering Mathematics. 1980;14:155-9.

[15] Hossain MA, Ahmed M. MHD forced and free convection boundary layer flow near the leading edge. International Journal of Heat and Mass Transfer. 1990;33:571-5.

[16] Alam S, Rahman M. Numerical Study of the Combined Free-Forced Convection and Mass Transfer Flow Past a Vertical Porous Plate in A Porous Medium With Heat Generation and Thermal Diffusion. Nonlinear Analysis: Modelling and Control. 2006;11:331-43.

[17] Sharma P, Singh G. Unsteady MHD free convective flow and heat transfer along a vertical porous plate with variable suction and internal heat generation. Int J Appl Math Mech. 2008;4.

[18] Abel MS, Siddheshwar PG, Mahesha N. Effects of thermal buoyancy and variable thermal conductivity on the MHD flow and heat transfer in a power-law fluid past a vertical stretching sheet in the presence of a non-uniform heat source. International Journal of Non-Linear Mechanics. 2009;44:1-12.

[19] Rahman MM, Roşca AV, Pop I. Boundary layer flow of a nanofluid past a permeable exponentially shrinking/stretching surface with second order slip using Buongiorno’s model. International Journal of Heat and Mass Transfer. 2014;77:1133-43.

[20] Seddeek M. The effect of variable viscosity on hydromagnetic flow and heat transfer past a continously porous boundary with radiation. International Communications in Heat and Mass Transfer. 2000;27:1037-46.

[21] Ali ME. The effect of variable viscosity on mixed convection heat transfer along a vertical moving surface. International

Journal of Thermal Sciences. 2006;45:60-9.

[22] Alam MS, Rahman MM, Sattar M. Transient Magnetohydrodynamic Free Convective Heat and Mass Transfer Flow with Thermophoresis past a Radiate Inclined Permeable Plate in the Presence of Variable Chemical Reaction and Temperature Dependent Viscosity. Nonlinear Analysis Modelling and Control. 2009;14(1):3-20.

[23] Rahman ATM, Alam MS, Alim MA, Chowdhury MK. Unsteady MHD Forced Convective Heat and Mass Transfer Flow along a Wedge with Variable Electric Conductivity and Thermophoresis. Procedia Engineering. 2013;56:531-7.

[24] Gupta S, Kumar D, Singh J. MHD mixed convective stagnation point flow and heat transfer of an incompressible nanofluid over an inclined stretching sheet with chemical reaction and radiation. International Journal of Heat and Mass Transfer. 2018;118:378-87.

[25] Sattar MA. A local similarity transformation for the unsteady two-dimensional hydrodynamic boundary layer equations of a flow past a wedge. International Journal of Applied Mathematics and Mechanics. 2011;7.

[26] Talbot L, Cheng RK, Schefer RW, Willis DR. Thermophoresis of particles in a heated boundary layer. Journal of Fluid Mechanics. 2006;101:737-58.

[27] Batchelor GK, Shen C. Thermophoretic deposition of particles in gas flowing over cold surfaces. Journal of Colloid and Interface Science. 1985;107:21-37.

[28] Sattar A, Hossain M. Unsteady hydromagnetic free convection flow with Hall current and mass transfer along an accelerated porous plate with time-dependent temperature and concentration. Canadian Journal of Physics. 2011;70:369-74.

[29] Rahman ATM, Alam MS, Uddin M. Influence of magnetic field and thermophoresis on transient forced convective heat and mass transfer flow along a porous wedge with variable thermal conductivity and variable Prandtl number. International Journal of Advances in Applied Mathematics and Mechanics. 2016;3:49-64.

[30] Alam MS, Sattar MA, Rahman MM, Postelnicu A. Local similarity solution of unsteady hydromagnetic convection flow of a micropolar fluid along a continuously moving permeable plate. International Journal of Heat and Technology. 2010;28:95-105.

[31] Nachtsheim PR, Swigert P. Satisfaction of asymptotic boundary conditions in numerical solution of systems of nonlinear equations of boundary layer-type. Washington, DC: National Aeronautics and Space Administration; 1965.

[32] White FM. Viscous Fluid Flows. Third Edition, McGraw-Hill, New York 2006.